

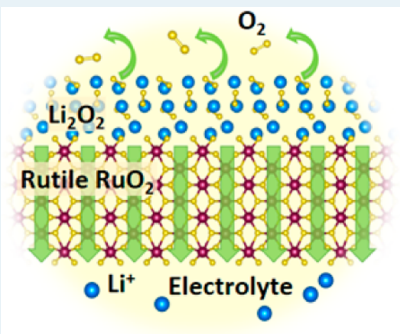
Unraveling the Catalytic Mechanism of Rutile RuO₂ for the Oxygen Reduction Reaction and Oxygen Evolution Reaction in Li–O₂ Batteries

Le Shi, Tianshou Zhao,* Ao Xu, and Zhaohuan Wei

Department of Mechanical and Aerospace Engineering, The Hong Kong University of Science and Technology, Clear Water Bay, Kowloon, Hong Kong

Supporting Information

ABSTRACT: Because of the involvement of solid-state discharge product Li₂O₂, how a catalyst works in nonaqueous lithium–oxygen batteries is yet to be determined, although the question has undergone fierce debate. In this work, we take an effective and widely used catalyst, rutile RuO₂, as a representative and studied its catalytic mechanism in lithium–oxygen batteries via *ab initio* calculations. For the oxygen reduction reaction (ORR), it is found that rutile RuO₂ can provide large adsorption energies toward LiO₂ and Li₂O₂, thus resulting in high initial discharge voltages. Moreover, the normalized degree of unsaturation of surface oxygen is identified as a descriptor for the ORR catalytic activity. For the oxygen evolution reaction (OER), we propose that, in addition to the three-phase interface, the OER may also occur at the two-phase interface of Li₂O₂/RuO₂, where rutile RuO₂ provides pathways for the lithium ions while oxygen evolves from the exposed surfaces of Li₂O₂. Calculation results show that our proposed catalytic scenario is both thermodynamically and kinetically viable. Along with the charge process, the remaining Li₂O₂ can be attracted to the catalytic surfaces spontaneously, which can effectively preserve the reaction interface.



KEYWORDS: nonaqueous lithium–oxygen batteries, rutile RuO₂, catalytic mechanism, density functional theory (DFT), oxygen reduction reaction (ORR), oxygen evolution reaction (OER)

1. INTRODUCTION

The development of nonaqueous lithium–oxygen batteries has attracted tremendous attention in recent years, because of the high theoretical capacity and energy density, which is several times greater than that of conventional lithium-ion batteries.^{1–7} However, at the current stage, nonaqueous lithium–oxygen batteries are suffering from many severe issues, such as sluggish reaction kinetics, high charging overpotential, and poor cycle life, which seriously impedes the commercialization process. Adding a catalyst to promote the related reactions has been proven to be an effective strategy to improve the reaction kinetics and lower the overpotential in many other energy storage systems.^{8–12} However, since the oxygen reduction reaction (ORR) and oxygen evolution reaction (OER) in nonaqueous lithium–oxygen batteries involve the accumulation and decomposition of the solid-state discharge product Li₂O₂, the situation become more complex.

For the ORR in nonaqueous lithium–oxygen batteries, it is now commonly agreed that before the catalytic surface is fully covered by Li₂O₂, a catalyst can influence the reaction through changing the energetics of reaction intermediates.^{13–15} Yet, for the OER, whether a catalyst works in this energy storage system, and how the catalyst works, are questions that have undergone fierce debate. In 2011, McCloskey et al.¹⁶ explored the performance of several typical catalysts in different

electrolytes, and found that, in the relatively stable electrolyte, catalysts did not show significant influence toward the discharge/charge voltage profiles. They proposed that the previously reported efficacy of catalysts in nonaqueous lithium–oxygen batteries mainly came from the decomposition of byproducts such as Li₂CO₃ and LiRCO₃, instead of Li₂O₂, and using catalysts may be unnecessary for nonaqueous lithium–oxygen batteries. However, in the following studies, researchers found that some catalysts, such as RuO₂^{17–19} and Co₃O₄^{20,21} could effectively catalyze the OER in nonaqueous lithium–oxygen batteries when employing a stable electrolyte. Many mechanisms have been proposed to justify the observed catalytic activity. Yilmaz et al.¹⁷ attributed the enhanced OER performance when employing RuO₂ as a catalyst to the good wettability between RuO₂ and Li₂O₂, which could induce a thin-film morphology of Li₂O₂, thus reducing the electronic resistance during the charge process. Black et al.²⁰ proposed that Co₃O₄ might facilitate the transportation of Li_{2-x}O₂ species on the surface of the electrode. Radin et al.²² found that the electronic/ionic conductivity of Li₂O₂ could be enhanced after being doped with metal cations such as Co²⁺, and proposed

Received: June 24, 2016

Revised: August 3, 2016

Published: August 15, 2016



that the enhanced electronic/ionic conductivity after doping is the reason for the observed lower charge overpotential. Zhu et al.^{23,24} constructed catalyst/Li₂O₂/O₂ interface models and identified that the surface acidity of a catalyst could be used as a descriptor for the OER catalytic activity. Yao et al.²⁵ proposed that Li₂O₂ might first react with the metal/metal oxide catalyst to form lithium metal oxide, and then undergo a delithiation process. Meini et al.²⁶ found that, in a nonaqueous lithium–oxygen battery system, trace amounts of water could influence the OER behavior significantly. They proposed that the water and/or redox mediator generated during the working process of the battery could facilitate the decomposition process of Li₂O₂. Most recently, Wang et al.²⁷ designed a solid-state battery system to exclude the possible influence of redox mediator. They found that, even in a solid-state environment, the Ru nanoparticles could still effectively lower the charge overpotential, and thus proposed that the catalysts could facilitate the OER through direct interaction with the discharge product, instead of redox mediator or dopants.

Clarifying the working mechanism of catalysts toward the ORR/OER is crucially important for rational catalyst design. In this work, we chose an effective and widely adopted catalyst, rutile RuO₂,^{17–19} as a representative, and we have studied its underlying catalytic mechanism for the ORR and OER in nonaqueous lithium–oxygen batteries, using density functional theory (DFT) calculation. Based on our previous work,²⁸ three exposed surfaces of rutile RuO₂—{001}, {101}, and {111}—were chosen to construct the reaction interfaces (exposed surface area in Wulff structure: {001} > {111} > {101}). For the discharge process, initial ORR and further nucleation of Li₂O₂ are discussed. A new descriptor, namely, the normalized degree of unsaturation of surface oxygen, is proposed for the ORR catalytic activity. For the charge process, three-phase interface (Li₂O₂/RuO₂/O₂) models were constructed. The {001} surface is found to show the highest catalytic activity toward the OER that occurs at the three-phase interface, with an equilibrium charge voltage as low as 3.08 V. Considering that, in realistic experiments, the area of such three-phase interface is quite limited, we propose a new catalytic scenario that the OER may also occur at the two-phase interface of Li₂O₂/RuO₂. In this new scenario, catalysts provide the reaction interface and, at the same time, function as a lithium ion conductor, while oxygen evolves from the exposed surfaces of Li₂O₂. The lithium-ion migration energy barrier in rutile RuO₂ was calculated to be as low as 0.21 eV. Two-phase interface models were constructed, and our proposed reaction route was identified to be thermodynamically viable. With this new catalytic mechanism, many previous experimental observations, such as the shrinkage of Li₂O₂ during the charge process,^{27,29} the efficacy of catalyst in solid-state environment,²⁷ and the valence state change for transition-metal catalysts during the charge process²⁵ can be perfectly explained.

2. COMPUTATIONAL DETAILS

First-principles calculations in this work were conducted using the ABINIT^{30–32} software package. Perdew–Burke–Ernzerhof (PBE) generalized gradient approximation (GGA)³³ was used for the exchange-correlation functional, and projector augmented wave (PAW) potential³⁴ was used to describe the ion-electron interaction. The cutoff energy for the plane-wave basis was set to be 20 Ha. The Monkhorst–Pack scheme³⁵ was employed for the *k*-point sampling, and the spacing between the *k*-point mesh was set to be <0.05 Å^{−1}. All the atoms were

fully relaxed with a force tolerance of 0.02 eV Å^{−1}. The Heyd–Scuseria–Ernzerhof (HSE) hybrid density functional^{36,37} implemented in the Quantum Espresso package³⁸ was employed to calculate the density of states (DOS), and one-quarter ($\alpha = 0.25$) of the local DFT exchange was replaced by the unscreened and nonlocal Fock exchange. The nudged elastic band (NEB) method was used to calculate the lithium migration energy barrier in the tunnels of rutile RuO₂.

Slab model adding vacuum layer was adopted in this work. The surface geometries were taken from our previous calculation results,²⁸ and the vacuum layer was thicker than 10 Å. All the surfaces employed are in a fully oxidized state and have been proven to be the most stable ones among all the terminations considered.²⁸ The adsorption energies of LiO₂ and Li₂O₂ were calculated using

$$E_{\text{ads}} = E_{\text{tot}}(S + A) - E_{\text{tot}}(A) - E_{\text{tot}}(S) \quad (1)$$

where $E_{\text{tot}}(S + A)$ is the total energy of the surface and adsorbate, $E_{\text{tot}}(A)$ is the total energy of the adsorbate and $E_{\text{tot}}(S)$ is the total energy of the surface. The adsorption energy of Li⁺+e[−] was calculated using

$$E_{\text{ads}} = E_{\text{tot}}(S + A) - E_{\text{tot}}(S) - \mu_{\text{Li}} \quad (2)$$

where μ_{Li} is the chemical potential of bulk lithium metal.

The reaction enthalpy change for the disproportionation reaction that occurs on the surfaces of rutile RuO₂ was calculated by³⁹

$$E_{\text{dis}} = E_{\text{Li}_2\text{O}_2 @\text{surf}} - 2E_{\text{LiO}_2 @\text{surf}} + E_{\text{surf}} + E_{\text{O}_2} \quad (3)$$

where E_{surf} , E_{O_2} , $E_{\text{LiO}_2 @\text{surf}}$ and $E_{\text{Li}_2\text{O}_2 @\text{surf}}$ is the total energy of the considered surface, the oxygen molecule, the considered surface adsorbed with LiO₂, and the considered surface adsorbed with Li₂O₂.

To address the well-known issue of oxygen overbinding in DFT calculations, the enthalpy of the oxygen molecule was calculated using the expression⁴⁰

$$H(T = 0 \text{ K}, \text{O}_2) = 2H(T = 0 \text{ K}, \text{O}) - \Delta E^{\text{exptl}} \quad (4)$$

where $H(T = 0 \text{ K})$ is the calculated zero-point energy of an oxygen atom or molecule, and ΔE^{exptl} is the binding energy of oxygen from experiments (5.12 eV).⁴⁰ The chemical potential of oxygen was calculated as

$$\mu_{\text{O}_2}(T, P_{\text{O}_2}) = H_{\text{O}_2}(0 \text{ K}) + \Delta H_{\text{O}_2}(T) - TS_{\text{O}_2}^{\text{exptl}}(T) + k_{\text{B}}T \ln \left(\frac{P_{\text{O}_2}}{P_{\text{O}_2}^0} \right) \quad (5)$$

where $\Delta H_{\text{O}_2}(T)$ is the enthalpy energy change from 0 K to temperature T , for which we used diatomic ideal gas approximation as $7/2k_{\text{B}}T$, and $S_{\text{O}_2}^{\text{exptl}}(T)$ is the entropy of oxygen at 1 atm obtained from experiments.⁴¹ $P_{\text{O}_2}^0$ was set to be 1 atm. The comparison between computational and experimental voltages of crystallized Li₂O, Li₂O₂, and LiO₂ are listed in Table S1 in the Supporting Information, and the values agree well.

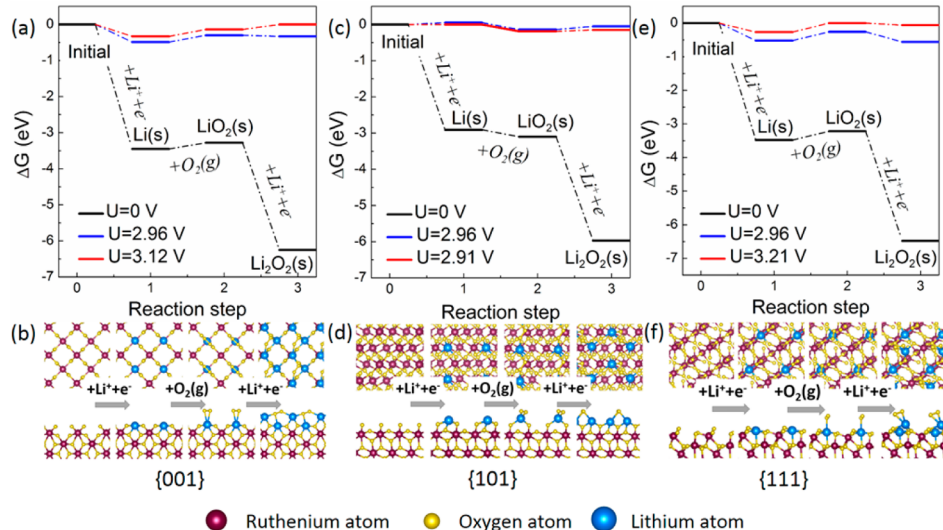
Energy profiles of the ORR/OER were obtained by adding/removing one lithium atom or oxygen molecule at each step. The reaction free energy of each step was calculated as

$$\Delta G = E - E_0 + \Delta N_{\text{Li}}(\mu_{\text{Li}} - eU) + \Delta N_{\text{O}_2}\mu_{\text{O}_2} \quad (6)$$

where E is the energy of considered slab model, E_0 is the energy of initial slab model, ΔN_{Li} and ΔN_{O_2} are the numbers of lithium

Table 1. Adsorption of $\text{Li}^+ + \text{e}^-$, LiO_2 , and Li_2O_2 on the {001}, {101}, and {111} Surface of Rutile RuO_2 .

coverage	RuO ₂ {001}		RuO ₂ {101}		RuO ₂ {111}	
	E_{ads} (eV)	$D_{\text{O-O}}$ (Å)	E_{ads} (eV)	$D_{\text{O-O}}$ (Å)	E_{ads} (eV)	$D_{\text{O-O}}$ (Å)
Adsorbate: $\text{Li}^+ + \text{e}^-$						
(1 × 1)	-3.45		-2.91		-3.48	
(1 × 1)	-2.42	1.24	-3.10	1.26	-3.22	1.23
(1 × 1)-1L	-3.26	1.29	-2.98	1.31	-3.50	1.26
(1 × 1)-2L	-3.07	1.41/1.40	-2.85	1.41/1.36	-3.41	1.29/1.28
(1 × 1)-3L	-2.99	1.46/1.44/1.40	-2.93	1.51/1.40/1.31	-3.20	1.49/1.33/1.29

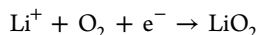
**Figure 1.** (a, c, e) Energy profiles and (b, d, f) geometries for the initial discharge process happened on the (a, b) {001} surface, (c, d) {101} surface, and (e, f) {111} surface of rutile RuO_2 .

atoms and oxygen molecules added/removed for each step, μ_{Li} and μ_{O_2} are the chemical potentials of bulk lithium and oxygen, respectively. The eU term was added to account for the electronic energy under an applied potential U . The overpotential was defined by shifting all the intermediates to $\Delta G < 0$, which is consistent with previous work.^{23,24,42}

3. RESULTS AND DISCUSSION

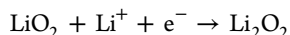
3.1. Initial Oxygen Reduction Reaction. It is now commonly agreed that the ORR in nonaqueous lithium–oxygen batteries contains two steps. At the first step, oxygen will get an electron and combine with a lithium ion to form lithium superoxide as

Step 1:



The formed LiO_2 then may either undergo another electrochemical reaction to form Li_2O_2 , as

Step 2.1:



or go through a chemical disproportionation reaction, as

Step 2.2:



The electrochemical reactions can only occur at the surface of electrode or catalyst, whereas the chemical disproportionation reaction can occur anywhere. From our calculation on the adsorption energies, as listed in Table 1, the adsorption energies for LiO_2 onto rutile RuO_2 surfaces are quite large. The large adsorption energies can effectively anchor the LiO_2 molecules onto the catalytic surfaces instead of letting them desorb into the electrolyte and go through a chemical disproportionation reaction there.^{43–45} Hence, in this work, we only considered that the ORR happened on the catalytic surfaces. By calculating the reaction enthalpy changes for the chemical disproportionation reaction that happened on the surfaces as eq 3, we found that all the reaction enthalpy changes are positive (0.57 eV for the {001} surface, 0.54 eV for the {101} surface, and 0.26 eV for the {111} surface). Thus, the disproportionation route is not favored for the ORR that happened on rutile RuO_2 surfaces.

We now consider the electrochemical reaction route. Since all of the surfaces exposed are oxygen-rich terminated, initial adsorption of oxygen is not favored.²⁸ Figures 1a, 1c, and 1e show the energy profiles for the initial ORR that happened on the three considered surfaces at the open-circuit potential ($U = 0$ V, black line), the equilibrium potential of bulk Li_2O_2 ($U = 2.96$ V, blue line), and the equilibrium potential for the initial discharge process, which could just keep all the reaction intermediates having a negative energy (red line). It can be found that, for all three surfaces considered, the initial ORR are thermodynamically favorable. The equilibrium voltages for the

ORR on {001}, {101}, and {111} surfaces are calculated to be 3.12, 2.91, and 3.21 V, respectively. The calculated high equilibrium initial discharge voltages for the {001} and {111} surfaces successfully explained the observed initial discharge voltages, which are higher than the equilibrium voltage of Li_2O_2 (2.96 V) in experiments.^{17–19} Figures 1b, 1d, and 1f show the corresponding geometry changes, along with the initial ORR reactions. In all of the cases, lithium atoms bond with the surface oxygen of rutile RuO_2 , and the oxygen atoms sit above the lithium atoms. Zheng et al.¹⁴ proposed that the surface oxygen density could be used as a descriptor for the ORR catalytic activity, where a higher oxygen density means more initial growth points and higher initial discharge voltage. However, in our calculation, we found that the surface oxygen density and the initial discharge voltage or the adsorption energy of Li_2O_2 do not show a positive correlation. We attribute this discrepancy to the different degrees of unsaturation for the surface oxygen at different surfaces. In the crystal structure of rutile RuO_2 , each oxygen atom is bonded to three surrounding Ru atoms. After surface cleavage, some of the Ru–O bonds were broken. The density of broken bonds determines the degree of unsaturation for the surface oxygen, which, at the same time, determines the ability for the surface to anchor Li_2O_2 . Hence, we define an indicator, namely, the normalized degree of unsaturation of surface oxygen (U_s) as follows:

$$U_s \equiv \frac{3N(\text{O}) - N(\text{Ru}-\text{O})_{\text{surf}}}{A_{\text{surf}}} \quad (7)$$

where $N(\text{O})$ is the number of surface oxygens, $N(\text{Ru}-\text{O})_{\text{surf}}$ is the number of Ru–O bonds connected to the surface oxygen, and A_{surf} is the surface area. We then plot the defined U_s against the initial discharge voltage and Li_2O_2 adsorption energy, as shown in Figure 2. It is found that U_s is a good descriptor for the initial discharge process, where a larger U_s means higher discharge voltage and stronger Li_2O_2 adsorption.

3.2. Growth of Li_2O_2 into Double and Triple Layers. As the discharge process continues, the exposed catalytic surfaces will be gradually covered by Li_2O_2 . Here, we have studied the adsorption behavior of double and triple layers of Li_2O_2 to gain further insight into the following discharge process. The

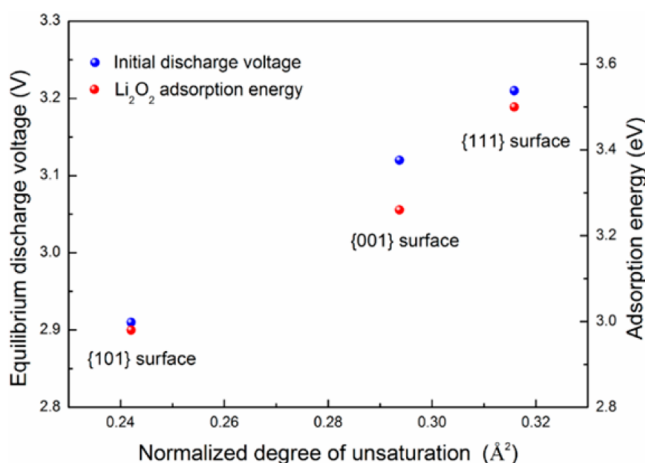


Figure 2. Relationship between the normalized degree of unsaturation, the initial equilibrium discharge voltage, and the adsorption energy of Li_2O_2 .

structures of multilayer adsorption model were obtained from making an analogy with the first layer deposited structure and then undergoing a fully geometrical optimization.³⁹ The adsorption energies and O–O bond lengths after more layers of Li_2O_2 adsorbed onto the three considered surfaces are listed in Table 1. The adsorption energies on these surfaces when more layers of Li_2O_2 are considered remain quite large, and the O–O bond lengths for the top layer Li_2O_2 deposited are significantly shorter than that in bulk Li_2O_2 (1.54 Å), exhibiting bond lengths closer to that of the superoxide ions (1.34 Å). When more layers of Li_2O_2 adsorbed onto the surfaces, the positive correlation between the U_s and adsorption energies was maintained.

The electronic properties for the Li_2O_2 adsorbed onto rutile RuO_2 surfaces were studied by calculating the density of states (DOS). To avoid the underestimation of the band gap, hybrid density functional (HSE06)^{36,37} was adopted. From Figure 3, all the Li_2O_2 adsorbed appeared to be conductive. The enhanced electronic conductivity will allow the growth of Li_2O_2 into a larger size and finally lead to a larger discharge capacity.

3.3. Oxygen Evolution Reaction Happened at the Interface of Crystalline $\text{Li}_2\text{O}_2/\text{RuO}_2/\text{O}_2$. In our previous work,²⁸ we constructed a three-phase interface model among the crystalline Li_2O_2 ($c\text{-Li}_2\text{O}_2$), $\text{RuO}_2\{001\}$ surface, and oxygen (represented by vacuum), following the approach presented by Zhu et al.^{23,24} In this work, we further constructed the three-phase interface model for the other two surfaces, the {101} and {111} surfaces, and studied the OER taken place at the three-phase interface. The comparison among the OER that happened on the three-phase interface for these three surfaces are shown in Figure 4. Figures 4 a, 4c, and 4e show the energy profiles, where the black line indicates the energy profile at the equilibrium voltage for the OER, following the route $\text{Li}^+ \rightarrow \text{Li}^+ \rightarrow \text{O}_2$ (route 1), and the red line indicates the energy profile at the equilibrium voltage for the OER, following the route $\text{Li}^+ \rightarrow \text{O}_2 \rightarrow \text{Li}^+$ (route 2). $\text{RuO}_2\{001\}$ was found to show the highest catalytic activity with an equilibrium charge voltage of 3.08 V toward route 1. In all of the cases, oxygen desorption was identified to be the rate-determining step, which is required to overcome large desorption energy barriers. The geometry changes along with the charge process are shown in Figures 4 b, 4d, and 4f. In all of the situations considered, the adsorbed Li_2O_2 has a tendency to leave the catalytic surfaces and the contact area between the catalyst and the discharge product decreases as the charge process continues. A quantitative analysis on the height changes of the center of mass for adsorbed Li_2O_2 are listed in Table 2. All the height changes for the $c\text{-Li}_2\text{O}_2/\text{RuO}_2/\text{O}_2$ model are positive, indicating a weak attraction between the catalytic surfaces and the adsorbed crystalline Li_2O_2 during the charge process.

3.4. Lithium Ion Transportation in the Tunnels of RuO_2 . Since the three-phase interface of $\text{Li}_2\text{O}_2/\text{RuO}_2/\text{O}_2$ is one-dimensional, its area is expected to be limited. Moreover, as observed in many experiments,^{17–19} during the discharge process, the rutile RuO_2 may be fully covered by Li_2O_2 , which further reduced the chance of appearance for the three-phase interface. For the exposed three-phase interface, according to the geometry changes mentioned above, after the initial consumption of the adsorbed Li_2O_2 , the rest Li_2O_2 would be in poor contact with the catalytic surfaces and the catalyst may become less effective, which is contradictory to previous experimental observations.^{17–19} A recent work done by Wang

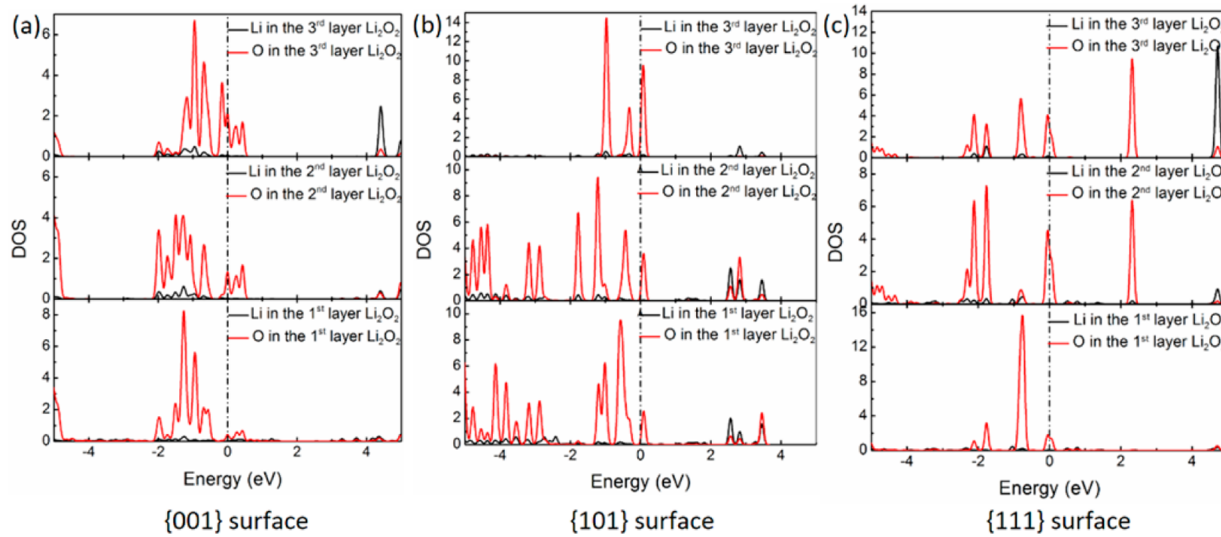


Figure 3. Density of states (DOS) for the Li_2O_2 after adsorption onto the (a) {001}, (b) {101}, and (c) {111} surface of rutile RuO_2 .

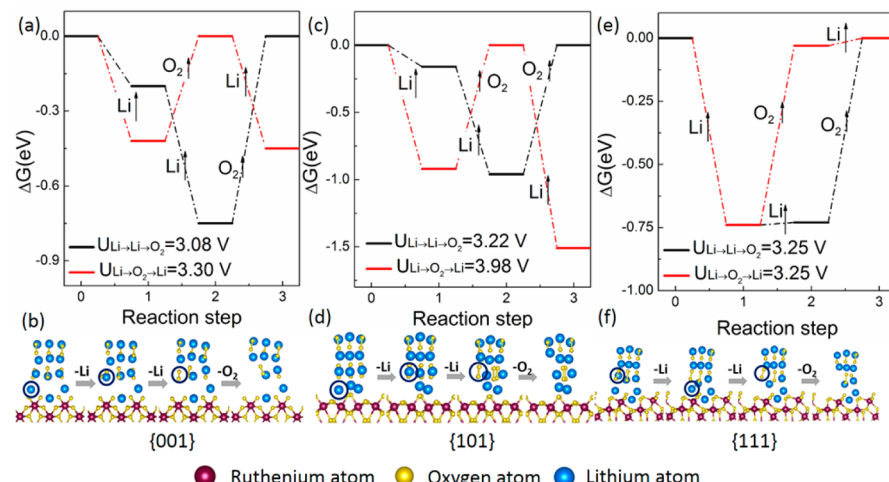


Figure 4. (a, c, e) Energy profiles and (b, d, f) geometries for the charge reaction happened on the three-phase interface of $c\text{-Li}_2\text{O}_2/\text{RuO}_2/\text{O}_2$: (a, b) {001} surface, (c, d) {101} surface, and (e, f) {111} surface. The blue circle indicates the atom/molecule to be removed in the next step.

Table 2. Height Change of the Center of Mass of Adsorbed Li_2O_2 for the Charge Reactions That Occurred on $c\text{-Li}_2\text{O}_2/\text{RuO}_2/\text{O}_2$, $c\text{-Li}_2\text{O}_2/\text{RuO}_2$, and $a\text{-Li}_2\text{O}_2/\text{RuO}_2$

	Δh (\AA)
$c\text{-Li}_2\text{O}_2/\text{RuO}_2/\text{O}_2$	
(001)	0.40
(101)	0.36
(111)	0.20
$c\text{-Li}_2\text{O}_2/\text{RuO}_2$	
(001)	-0.68
(101)	-0.44
(111)	-0.82
$a\text{-Li}_2\text{O}_2/\text{RuO}_2$	
(001)	-0.56
(101)	-0.18
(111)	-0.27

et al.²⁷ shows that Ru nanoparticles could exhibit catalytic activity in a solid-state environment where the three-phase interface considered above does not exist. Combined with previous experimental observation of the shrinkage of

Li_2O_2 ^{27,29} and the valence state change of the transition-metal oxide catalyst²⁵ during the OER, the three-phase interface model may not comprehensively describe the OER that occurred on the catalytic surfaces. Since rutile RuO_2 can conduct lithium ions and has been used as anode in lithium-ion batteries,⁴⁶ we start to explore the possibility that, during the charge process, lithium ions are being conducted out through the rutile RuO_2 nanoparticles while oxygen evolved from the exposed surfaces of Li_2O_2 , as illustrated in Figure 5b. Compared with the conventional three-phase interface reaction as shown in Figure 5a, the catalyst's capability to conduct lithium ions could greatly enlarge the reaction interface.

Rutile RuO_2 has one-dimensional (1D) tunnels in its crystal structure, as shown in Figure 6a, which provides transportation pathways for the lithium ions. We calculated the lithium ion migration energy barriers along the tunnels at different lithium ion concentrations, using supercells with different sizes. The energy profiles for the migration process are shown in Figure 6b. For the $1 \times 1 \times 2$ supercell, which corresponds to a lithium ion concentration of $\text{Li}_{0.5}\text{RuO}_2$, the migration energy barrier is 0.25 eV, and when using a larger $2 \times 2 \times 2$ supercell ($\text{Li}_{0.125}\text{RuO}_2$), the migration energy barrier reduced to be 0.21

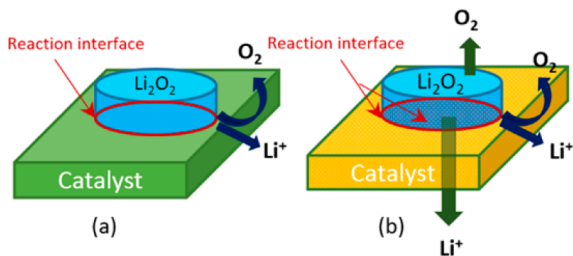


Figure 5. Illustration for the catalytic mechanism of (a) catalysts that cannot conduct lithium ions and (b) catalysts that can conduct lithium ions.

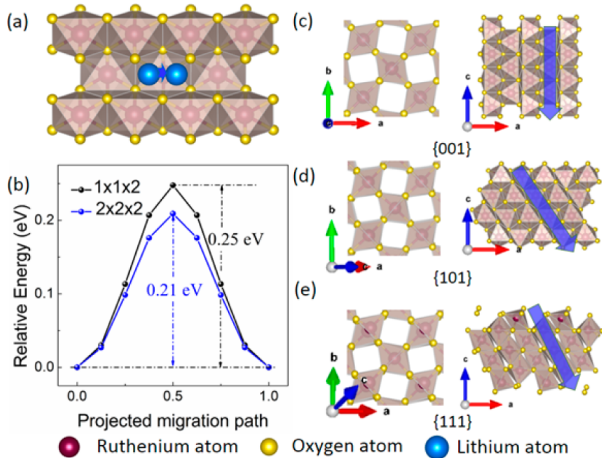


Figure 6. (a) Lithium ion migration path in the tunnels of rutile RuO_2 . (b) Energy profiles along the path shown in panel (a). Schematics showing the tunnel openings exposed on (c) the $\{001\}$ surface, (d) the $\{101\}$ surface, and (e) the $\{111\}$ surface.

eV. These results are consistent with previous calculations.⁴⁷ The relatively low migration energy barrier enables rutile RuO_2 to serve as a lithium ion conductor during the charge process, and the lithium ion conductivity in rutile RuO_2 is expected to be larger than that in both the crystalline and amorphous Li_2O_2 .^{48,49} It is also worth noting that, for all the three surfaces studied, there exist openings to access the tunnels, as shown in Figures 6 c, 6d, and 6e. In the experiments,^{17–19} the size of

rutile RuO_2 nanoparticles employed is usually <5 nm, and this short migration distance enables the lithium ions to transport out to the electrolyte easily. Many of the previously reported catalysts in nonaqueous lithium–oxygen batteries, such as MoO_3 ,²⁵ Cr_2O_3 ,²⁵ and Co_3O_4 ^{20,21} are also lithium ions conductors and have been used as anode materials in lithium-ion batteries.^{50–52} In addition, our group has successfully developed a series of solid-state lithium–oxygen/air batteries employing LATP as electrolyte,^{53–55} and has achieved excellent battery performance. These facts further supported our proposed catalytic scenario.

During the charge process, the lithium ions may be conducted out directly through the catalysts, as calculated above, or the lithium ions may insert into the catalyst to form a lithium metal oxide phase first, then undergo a delithiation process, as proposed by Yao et al.,²⁵ depending on the specific thermodynamic/kinetic properties. For the oxygen release process, two possible routes are proposed:

- (1) After one lithium atom at the interface migrated out through the catalyst, a lithium vacancy will be generated spontaneously. The newly generated lithium vacancy can pop up to the exposed surfaces of Li_2O_2 , which is supported by previous calculations and experiments,^{48,49,56} making the exposed surface oxygen-rich; thus, oxygen can evolve from the exposed surfaces of Li_2O_2 easily (as shown in Figure S1.a in the Supporting Information)
- (2) It is also possible that lithium ions can be conducted out continuously to form a $\text{Li}_{2-x}\text{O}_2$ phase before oxygen release, as suggested by Kang et al.,⁵⁷ rendering the discharge product more conductive,^{43,58,59} and the left $\text{Li}_{2-x}\text{O}_2$ phase further decomposed to lithium ions and oxygen molecules (as shown in Figure S1.b in the Supporting Information)

3.5. Oxygen Evolution Reaction That Occurred at the Crystalline $\text{Li}_2\text{O}_2/\text{RuO}_2$ Interface. In this section, we tried to explore the thermodynamic feasibility of our proposed mechanism using the models built in section 3.3. This time, the lithium ion at the two-phase interface of $c\text{-Li}_2\text{O}_2/\text{RuO}_2$ was taken away first, then, similar to that in the three-phase interface reaction, we considered two possible routes as $\text{Li}^+ \rightarrow$

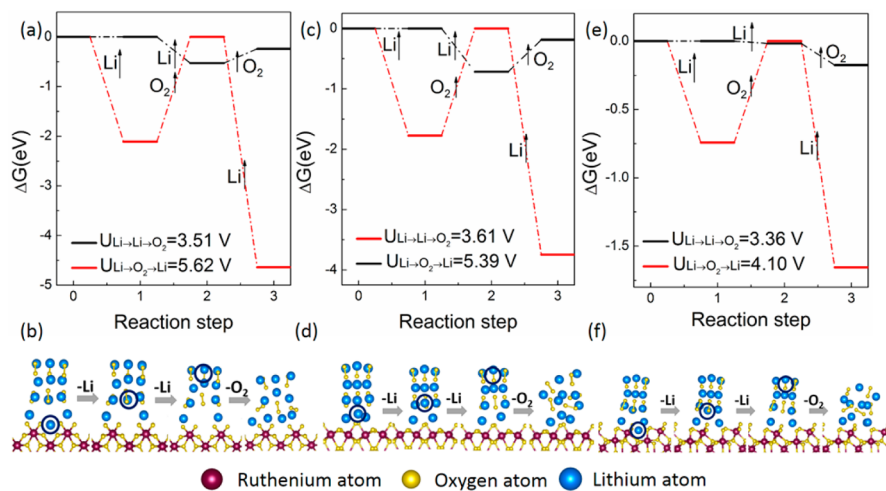


Figure 7. (a, c, e) Energy profiles and (b, d, f) geometries for the charge reaction that occurred at the $c\text{-Li}_2\text{O}_2/\text{RuO}_2$ interface: (a, b) $\{001\}$ surface, (c, d) $\{101\}$ surface, and (e, f) $\{111\}$ surface. The blue circle indicates the atom/molecule to be removed in the next step.

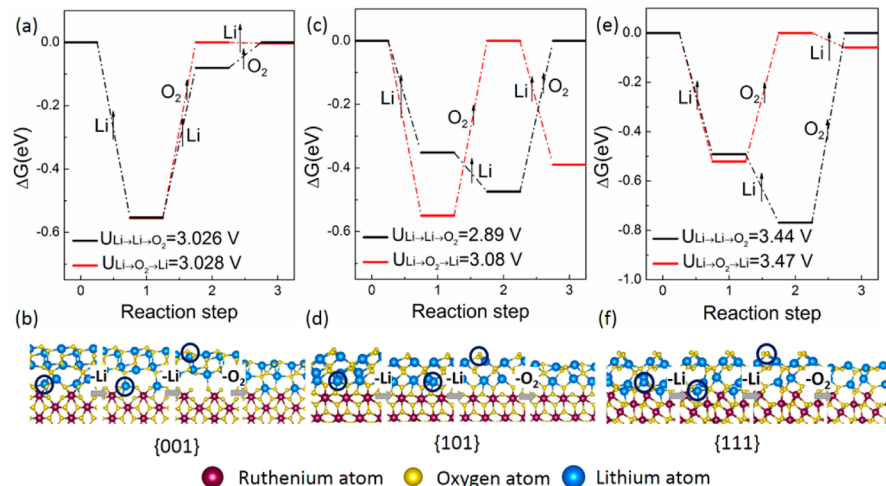


Figure 8. (a, c, e) Energy profiles and (b, d, f) geometries for the charge reaction happened at the $a\text{-Li}_2\text{O}_2/\text{RuO}_2$ interface: (a, b) $\{001\}$ surface, (c, d) $\{101\}$ surface, and (e, f) $\{111\}$ surface. The blue circle indicates the atom/molecule to be removed in the next step.

$\text{Li}^+ \rightarrow \text{O}_2$ (route 1) and $\text{Li}^+ \rightarrow \text{O}_2 \rightarrow \text{Li}^+$ (route 2). At the oxygen evolution step, one oxygen molecule at the exposed $\{001\}$ surface of Li_2O_2 was removed. The energy profiles for the OER that occurred following our proposed reaction mechanism are shown in Figures 7a, 7c, and 7e. For all the three surfaces, route 1 shows the lower equilibrium charge voltage. The calculated equilibrium charge voltage for the OER on the $\{001\}$, $\{101\}$, and $\{111\}$ surfaces are 3.51, 3.61, and 3.36 V, respectively, which are slightly higher than those at the three-phase interface and in good agreement with experimental observations.²⁷ Different from the OER that occurred at the three-phase interface, lithium desorption become the rate-limiting step. The geometry changes during the OER are shown in Figures 7b, 7d, and 7f. After the removal of one unit of Li_2O_2 in our proposed sequence, the crystal structure of adsorbed Li_2O_2 collapsed to some extent and the remaining Li_2O_2 remained in good contact with the catalytic surfaces. The height change of the center of mass of adsorbed Li_2O_2 is negative, as listed in Table 2, indicating that the catalytic surfaces could attract the remaining Li_2O_2 spontaneously during the OER process.

3.6. Oxygen Evolution Reaction That Occurred at the Interface of Amorphous $\text{Li}_2\text{O}_2/\text{RuO}_2$. Since the lattice mismatches between Li_2O_2 and the considered surfaces of rutile RuO_2 are quite large, it is highly possible that the Li_2O_2 near the catalytic surfaces is amorphous instead of crystalline. In this section, we studied the OER following our proposed mechanism in a two-phase interface model of amorphous Li_2O_2 ($a\text{-Li}_2\text{O}_2$)/ RuO_2 . The initial geometry of $a\text{-Li}_2\text{O}_2/\text{RuO}_2$ was taken from the adsorption model of three layers of Li_2O_2 onto rutile RuO_2 . Compared with the amorphous structure of Li_2O_2 generated from melt-and-quench procedure,⁴⁸ we believe that the structure obtained from the adsorption process is closer to the realistic situation. In these models, the lithium and oxygen atoms do not align orderly as in the crystallized structure; instead, they stack together without long-range order. For this reason, we call them “amorphous state” to differentiate from the “crystallized state”. One lithium atom at the interface nearest to the tunnel openings was taken away first, then the two OER routes described in sections 3.3 and 3.5 were considered. One oxygen molecular at the top layer of adsorbed Li_2O_2 was removed at the oxygen evolution step. From Figures

8a, 8c, and 8e, in all cases, the first route is more favorable. Similar to that in the $c\text{-Li}_2\text{O}_2/\text{RuO}_2/\text{O}_2$, oxygen desorption is the rate-determining step, which shows large desorption energy barriers to be overcome.

The trend for the OER equilibrium voltage of different surfaces is the same as the initial ORR equilibrium voltage, where the $\{101\}$ surface shows the lowest voltage (2.89 V), the $\{001\}$ surface shows a medium voltage (3.03 V), and the $\{111\}$ surface shows the highest voltage (3.44 V). For the $\{001\}$ surface and the $\{101\}$ surface, the equilibrium charge voltages for reactions that occurred on the two-phase interface of $a\text{-Li}_2\text{O}_2/\text{RuO}_2$ are lower than those happened on the three-phase interface of $c\text{-Li}_2\text{O}_2/\text{RuO}_2/\text{O}_2$, and also are lower than those happened on many surfaces of crystalline Li_2O_2 .⁴² The geometry changes, along with the charge process, is shown in Figures 8b, 8d, and 8e. Similar to that which occurred at the $c\text{-Li}_2\text{O}_2/\text{RuO}_2$ interface, the adsorbed Li_2O_2 approaches the catalytic surfaces spontaneously, which has been further validated through the height change of the center of mass, as listed in Table 2.

4. CONCLUSION

In this work, we provided a comprehensive first-principles investigation of the underlying oxygen reduction reaction (ORR) and oxygen evolution reaction (OER) catalytic mechanism in nonaqueous lithium–oxygen batteries, using a representative catalyst rutile RuO_2 . The calculation results show that the exposed surfaces of rutile RuO_2 exhibit strong adsorption toward the reaction intermediate LiO_2 and reaction product Li_2O_2 , which can effectively confine the ORR to occur on the catalytic surfaces, instead of happening in the electrolyte. Compared to the chemical disproportionation reaction route, the electrochemical reaction route is more favored. The normalized degree of unsaturation of surface oxygen was identified as a descriptor for the catalytic activity, and a higher normalized degree of unsaturation means a higher initial discharge voltage, as well as a larger adsorption energy toward Li_2O_2 . Three-phase interface models of $\text{Li}_2\text{O}_2/\text{RuO}_2/\text{O}_2$ were built, and the $\{001\}$ surface was identified to show the highest catalytic activity for the OER reaction, with an equilibrium voltage of 3.08 V.

Considering the fact that the area of the three-phase interface is quite limited and conventional three-phase interface model cannot explain many experimental observations satisfactorily,^{25,27,29} we proposed a new catalytic scenario that lithium ions are being conducted through the catalyst while oxygen evolves from the exposed surfaces of Li_2O_2 . This newly proposed catalytic mechanism is supported by our calculations on the lithium migration energy barrier in rutile RuO_2 , and the energy profiles for the OER follow our proposed mechanism at the two-dimensional interface of both $c\text{-Li}_2\text{O}_2/\text{RuO}_2$ and $a\text{-Li}_2\text{O}_2/\text{RuO}_2$. Different from the OER on the three-phase interface, the remaining Li_2O_2 can be attracted to the catalytic surfaces spontaneously during the charge process, following our proposed route, which maintained the reaction interface and explained the observed efficacy of catalyst during the entire charge process.^{17–19,27} Our work provided fundamental insight into the underlying working mechanism of catalysts in nonaqueous lithium–oxygen batteries and advanced the steps toward rational catalyst design.

■ ASSOCIATED CONTENT

Supporting Information

The Supporting Information is available free of charge on the ACS Publications website at DOI: [10.1021/acscatal.6b01778](https://doi.org/10.1021/acscatal.6b01778).

Computational and experimental voltages for Li_2O , Li_2O_2 , and LiO_2 ; proposed routes for oxygen release ([PDF](#))

■ AUTHOR INFORMATION

Corresponding Author

*Tel.: (852) 2358 8647. E-mail: metzhao@ust.hk (T. S. Zhao).

Notes

The authors declare no competing financial interest.

■ ACKNOWLEDGMENTS

The work described in this paper was fully supported by a grant from the Research Grants Council of the Hong Kong Special Administrative Region, China (Project No. 16213414).

■ REFERENCES

- (1) Luntz, A. C.; McCloskey, B. D. *Chem. Rev.* **2014**, *114*, 11721–11750.
- (2) Park, M.; Sun, H.; Lee, H.; Lee, J.; Cho, J. *Adv. Energy Mater.* **2012**, *2*, 780–800.
- (3) Wang, J.; Li, Y.; Sun, X. *Nano Energy* **2013**, *2*, 443–467.
- (4) Peng, Z.; Freunberger, S. A.; Chen, Y.; Bruce, P. G. *Science* **2012**, *337*, 563–566.
- (5) Rahman, M. A.; Wang, X.; Wen, C. *J. Appl. Electrochem.* **2014**, *44*, 5–22.
- (6) Lu, Y. C.; Gallant, B. M.; Kwabi, D. G.; Harding, J. R.; Mitchell, R. R.; Whittingham, M. S.; Shao-Horn, Y. *Energy Environ. Sci.* **2013**, *6*, 750–768.
- (7) Shi, L.; Zhao, T. S. *Sci. Bull.* **2015**, *60*, 281–282.
- (8) Zhou, X. J.; Qiao, J. L.; Yang, L.; Zhang, J. J. *Adv. Energy Mater.* **2014**, *4* (8), 1301523.
- (9) Liew, K. B.; Daud, W. R.; Ghasemi, M.; Leong, J. X.; Lim, S. S.; Ismail, M. *Int. J. Hydrogen Energy* **2014**, *39*, 4870–4883.
- (10) Nagai, T.; Yamazaki, S. I.; Fujiwara, N.; Asahi, M.; Siroma, Z.; Ioroi, T. *J. Electrochem. Soc.* **2016**, *163*, F347–F352.
- (11) Li, B.; Gu, M.; Nie, Z.; Wei, X.; Wang, C.; Sprenkle, V.; Wang, W. *Nano Lett.* **2014**, *14*, 158–165.
- (12) Wang, W.; Luo, Q.; Li, B.; Wei, X.; Li, L.; Yang, Z. *Adv. Funct. Mater.* **2013**, *23*, 970–986.
- (13) Kim, H. J.; Jung, S. C.; Han, Y. K.; Oh, S. H. *Nano Energy* **2015**, *13*, 679–686.
- (14) Zheng, Y.; Song, K.; Jung, J.; Li, C.; Heo, Y. U.; Park, M. S.; Cho, M.; Kang, Y. M.; Cho, K. *Chem. Mater.* **2015**, *27*, 3243–3249.
- (15) Dathar, G. K.; Shelton, W. A.; Xu, Y. *J. Phys. Chem. Lett.* **2012**, *3*, 891–895.
- (16) McCloskey, B. D.; Scheffler, R.; Speidel, A.; Bethune, D. S.; Shelby, R. M.; Luntz, A. C. *J. Am. Chem. Soc.* **2011**, *133*, 18038–18041.
- (17) Yilmaz, E.; Yogi, C.; Yamanaka, K.; Ohta, T.; Byon, H. R. *Nano Lett.* **2013**, *13*, 4679–4684.
- (18) Jian, Z.; Liu, P.; Li, F.; He, P.; Guo, X.; Chen, M.; Zhou, H. *Angew. Chem., Int. Ed.* **2014**, *53*, 442–446.
- (19) Jung, H. G.; Jeong, Y. S.; Park, J. B.; Sun, Y. K.; Scrosati, B.; Lee, Y. J. *ACS Nano* **2013**, *7*, 3532–3539.
- (20) Black, R.; Lee, J. H.; Adams, B.; Mims, C. A.; Nazar, L. F. *Angew. Chem.* **2013**, *125*, 410–414.
- (21) Ryu, W. H.; Yoon, T. H.; Song, S. H.; Jeon, S.; Park, Y. J.; Kim, I. D. *Nano Lett.* **2013**, *13*, 4190–4197.
- (22) Radin, M. D.; Monroe, C. W.; Siegel, D. J. *Chem. Mater.* **2015**, *27*, 839–847.
- (23) Zhu, J.; Ren, X.; Liu, J.; Zhang, W.; Wen, Z. *ACS Catal.* **2015**, *5*, 73–81.
- (24) Zhu, J.; Wang, F.; Wang, B.; Wang, Y.; Liu, J.; Zhang, W.; Wen, Z. *J. Am. Chem. Soc.* **2015**, *137*, 13572–13579.
- (25) Yao, K. P.; Risch, M.; Sayed, S. Y.; Lee, Y. L.; Harding, J. R.; Grimaud, A.; Pour, N.; Xu, Z.; Zhou, J.; Mansour, A.; Bardé, F.; Shao-Horn, Y. *Energy Environ. Sci.* **2015**, *8*, 2417–2426.
- (26) Meini, S.; Solchenbach, S.; Piana, M.; Gasteiger, H. A. *J. Electrochem. Soc.* **2014**, *161*, A1306–A1314.
- (27) Wang, Y.; Liang, Z.; Zou, Q.; Cong, G.; Lu, Y. C. *J. Phys. Chem. C* **2016**, *120*, 6459–6466.
- (28) Shi, L.; Xu, A.; Zhao, T. S. *J. Phys. Chem. C* **2016**, *120*, 6356–6362.
- (29) Zheng, H.; Xiao, D.; Li, X.; Liu, Y.; Wu, Y.; Wang, J.; Jiang, K.; Chen, C.; Gu, L.; Wei, X.; Hu, Y. S.; Chen, Q.; Li, H. *Nano Lett.* **2014**, *14*, 4245–4249.
- (30) Gonze, X.; Beuken, J. M.; Caracas, R.; Detraux, F.; Fuchs, M.; Rignanese, G. M.; Sindic, L.; Verstraete, M.; Zerah, G.; Jollet, F.; Torrent, M.; Roy, A.; Mikami, M.; Ghosez, Ph.; Raty, J.-Y.; Allan, D. C. *Comput. Mater. Sci.* **2002**, *25*, 478–492.
- (31) Gonze, X.; Amadon, B.; Anglade, P. M.; Beuken, J. M.; Bottin, F.; Boulanger, P.; Bruneval, F.; Caliste, D.; Caracas, R.; Cote, M.; Deutsch, T.; et al. *Comput. Phys. Commun.* **2009**, *180*, 2582–2615.
- (32) Gonze, X. Z. *Kristallogr. - Cryst. Mater.* **2005**, *220*, 558–562.
- (33) Perdew, J. P.; Burke, K.; Ernzerhof, M. *Phys. Rev. Lett.* **1996**, *77*, 3865.
- (34) Blöchl, P. E. *Phys. Rev. B: Condens. Matter Mater. Phys.* **1994**, *50*, 17953.
- (35) Monkhorst, H. J.; Pack, J. D. *Phys. Rev. B* **1976**, *13*, 5188.
- (36) Heyd, J.; Scuseria, G. E.; Ernzerhof, M. *J. Chem. Phys.* **2003**, *118*, 8207–8215.
- (37) Paier, J.; Marsman, M.; Hummer, K.; Kresse, G.; Gerber, I. C.; Ángyán, J. G. *J. Chem. Phys.* **2006**, *124*, 154709.
- (38) Giannozzi, P.; Baroni, S.; Bonini, N.; Calandra, M.; Car, R.; Cavazzoni, C.; Ceresoli, D.; Chiarotti, G. L.; Cococcioni, M.; Dabo, I.; Dal Corso, A.; et al. *J. Phys.: Condens. Matter* **2009**, *21*, 395502.
- (39) Geng, W. T.; Ohno, T. *J. Phys. Chem. C* **2015**, *119*, 1024–1031.
- (40) Radin, M. D.; Rodriguez, J. F.; Tian, F.; Siegel, D. J. *J. Am. Chem. Soc.* **2012**, *134*, 1093–1103.
- (41) Stull, D. R.; Prophet, H. *JANAF Thermochemical Tables*; National Standard Reference Data System; U.S. National Bureau of Standards: Washington, DC, 1971.
- (42) Mo, Y.; Ong, S. P.; Ceder, G. *Phys. Rev. B: Condens. Matter Mater. Phys.* **2011**, *84*, 205446.
- (43) Zhai, D.; Wang, H. H.; Yang, J.; Lau, K. C.; Li, K.; Amine, K.; Curtiss, L. A. *J. Am. Chem. Soc.* **2013**, *135*, 15364–15372.
- (44) Johnson, L.; Li, C.; Liu, Z.; Chen, Y.; Freunberger, S. A.; Ashok, P. C.; Praveen, B. B.; Dholakia, K.; Tarascon, J. M.; Bruce, P. G. *Nat. Chem.* **2014**, *6*, 1091–1099.

- (45) Tan, P.; Shi, L.; Shyy, W.; Zhao, T. S. *Energy Technol.* **2016**, *4*, 393–400.
- (46) Balaya, P.; Li, H.; Kienle, L.; Maier, J. *Adv. Funct. Mater.* **2003**, *13*, 621–625.
- (47) Jung, J.; Cho, M.; Zhou, M. *AIP Adv.* **2014**, *4*, 017104.
- (48) Radin, M. D.; Siegel, D. J. *Energy Environ. Sci.* **2013**, *6*, 2370–2379.
- (49) Tian, F.; Radin, M. D.; Siegel, D. J. *Chem. Mater.* **2014**, *26*, 2952–2959.
- (50) Hu, J.; Li, H.; Huang, X.; Chen, L. *Solid State Ionics* **2006**, *177*, 2791–2799.
- (51) Meduri, P.; Clark, E.; Kim, J. H.; Dayalan, E.; Sumanasekera, G. U.; Sunkara, M. K. *Nano Lett.* **2012**, *12*, 1784–1788.
- (52) Yu, A.; Park, H. W.; Davies, A.; Higgins, D. C.; Chen, Z.; Xiao, X. *J. Phys. Chem. Lett.* **2011**, *2*, 1855–1860.
- (53) Zhu, X. B.; Zhao, T. S.; Wei, Z. H.; Tan, P.; Zhao, G. *Energy Environ. Sci.* **2015**, *8*, 2782–2790.
- (54) Zhu, X. B.; Zhao, T. S.; Wei, Z. H.; Tan, P.; An, L. *Energy Environ. Sci.* **2015**, *8*, 3745–3754.
- (55) Zhu, X. B.; Zhao, T. S.; Tan, P.; Wei, Z. H.; Wu, M. C. *Nano Energy* **2016**, *26*, 565–576.
- (56) Dunst, A.; Epp, V.; Hanzu, I.; Freunberger, S. A.; Wilkening, M. *Energy Environ. Sci.* **2014**, *7*, 2739–2752.
- (57) Kang, S.; Mo, Y.; Ong, S. P.; Ceder, G. *Chem. Mater.* **2013**, *25*, 3328–3336.
- (58) Viswanathan, V.; Thygesen, K. S.; Hummelshøj, J. S.; Nørskov, J. K.; Girishkumar, G.; McCloskey, B. D.; Luntz, A. C. *J. Chem. Phys.* **2011**, *135*, 214704.
- (59) Shi, L.; Xu, A.; Zhao, T. S. *Phys. Chem. Chem. Phys.* **2015**, *17*, 29859–29866.